Measured band splitting supports Weyl nodes in fully polarized CeBi

Yu Liu,[1] Christian E. Matt,[1] Harris Pirie,[1] Nathan C. Drucker,[2] Na Hyun Jo,[3,4] Brinda Kuthanazhi,[3,4] Zhao Huang,[5] Christopher Lane,[5,6] Gunnar F. Lange,[7] Robert-Jan Slager,[7] Jian-Xin Zhu,[5,6] Paul C. Canfield,[3,4] and Jennifer E. Hoffman[1,2,*]

[1] *Department of Physics, Harvard University, Cambridge, Massachusetts 02138, USA*
[2] *School of Engineering & Applied Sciences, Harvard University, Cambridge, Massachusetts 02138, USA*
[3] *Ames Laboratory, Iowa State University, Ames, Iowa 50011, USA*
[4] *Department of Physics and Astronomy, Iowa State University, Ames, Iowa 50011, USA*
[5] *Theoretical Division, Los Alamos National Laboratory, Los Alamos, New Mexico 87545, USA*
[6] *Center for Integrated Nanotechnology, Los Alamos National Laboratory, Los Alamos, New Mexico 87545, USA*
[7] *TCM Group, Cavendish Laboratory, University of Cambridge, J.J. Thomson Avenue, Cambridge CB3 0HE, United Kingdom*

(Dated: February 20, 2023)

CeBi is predicted to be a tunable Weyl semimetal, in which the existence, energy, and momentum of Weyl points can be controlled by applying a magnetic field to change its spin ordering phase. In the fully-polarized phase with sufficient band spitting, two sets of Weyl points are predicted along the magnetic field axis. Here we use scanning tunneling microscopy and spectroscopy to directly measure the band splitting and surface states. By comparing quasiparticle interference maps of CeBi at $B = 0$ T and $B = 9$ T, we discover that the outer Bi $6p$ band is split by ~ 200 meV on the (001) surface in the fully-polarized phase, which is sufficient to overcome the hybridization gap and give rise to the predicted Weyl state. Additionally, we observe three sets of surface states whose consistency with our slab calculation in fully-polarized CeBi further supports our full theoretical picture of a Weyl state. Our findings confirm the possibility of driving CeBi between different topological phases with a magnetic field.

I. INTRODUCTION

1 **[Intro to magnetic Weyl semimetal]** A Weyl semimetal arises when a bulk Dirac cone is split into two Weyl cones of opposite chirality by breaking either inversion or time-reversal symmetry (TRS) [1]. The bulk Weyl nodes are connected by surface Fermi arcs that give rise to extraordinary properties including the chiral anomaly [2], negative magnetoresistance [2, 3], anomalous Hall effect [4, 5], and anomalous Nernst effect [6, 7]. Those properties, together with the high electron mobility, make Weyl semimetals promising for applications in spintronics and ultra fast optoelectronics [8, 9]. Magnetism offers an extra knob to tune the presence and separation of the Weyl nodes, and the resulting electronic properties [10]. Magnetic Weyl semimetals have been realized in antiferromagnetic GdPtBi [4] and Mn_3Sn [11] as well as ferromagnetic $Co_3Sn_2S_2$ [12, 13] and Co_2MnGa [14]. The possibility of manipulating the Weyl nodes with external magnetic field in Weyl semimetals have been tested by many transport studies [6, 11, 15–17]. Recent angle-resolved photoemission spectroscopy (ARPES) studies [18, 19] have shown that temperature can be used to induce a topological phase transition in $Co_3Sn_2S_2$ between its paramagnetic phase with no Weyl node and ferromagnetic phase with two pairs of Weyl nodes, which makes it a temperature tuned magnetic Weyl semimetal. However, there still lacks spectroscopic studies on the magnetic field control of a tunable magnetic Weyl semimetal.

2 **[Intro to CeBi]** CeBi possesses the two key ingredients of a tunable magnetic Weyl semimetal: nontrivial band topology and a rich magnetic phase diagram that enables tuning between different topological states. First, nontrivial Z_2 band topology arises when the Ce $5d$ and Bi $6p$ bands are inverted by strong spin-orbit coupling. This band inversion has been predicted by density functional theory (DFT) [20] and verified by ARPES [21–24]. Second, the rich magnetic phase diagram of CeBi, shown in Fig. 1(a), has been cataloged by magnetization, transport, and thermal measurements [25–27]. As an applied magnetic field tunes CeBi from the antiferromagnetic (++−−) to ferrimagnetic (+++−) to fully polarized (++++) states, the inverted Ce $5d$ and Bi $6p$ bands are predicted by DFT to split and cross again, giving rise to several evolving Weyl nodes [28, 29]. In the intermediate (+++−) phase of CeBi, band splitting of ~ 100 meV was verified by quasiparticles interference (QPI) imaging [29], supporting the existence of multiple Weyl nodes, however band folding complicates their visualization. The high-field (++++) state offers a simpler structure with four predicted Weyl nodes whose separation may be determined by the band splitting, and tuned by externally applied magnetic field. However, the band structure and splitting in the high-field (++++) state of CeBi has not been experimentally explored.

3 **[Here we show 200 meV splitting...]** Here we use scanning tunneling microscopy (STM) and quasiparticle interference (QPI) imaging to quantify the band structure and splitting in the fully-polarized phase of CeBi. Our DFT calculation shows that in the (++++) state, when the combined band splitting of the outer Bi $6p$ band

* jhoffman@physics.harvard.edu

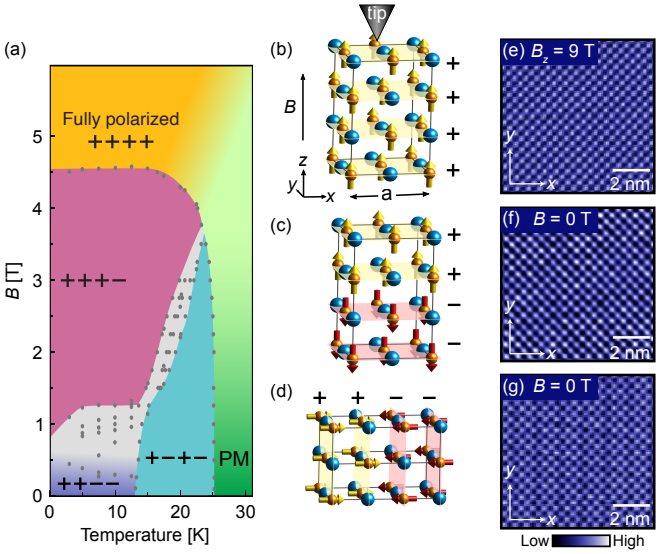

FIG. 1. (a) Magnetic phase diagram of bulk CeBi measured by magneto-transport [27]. (b-d) Crystal structures of (b) fully polarized (++++) CeBi in the (001) orientation, and (++−−) phase in the (c) (001) and (d) (010) orientations. (e-g) STM topographies of CeBi correspond to the magnetic states and orientations of (b-d). Setup conditions: (e) Sample bias $V_s = 200$ mV, current setpoint $I_s = 2$ nA with an external magnetic field $B_z = 9$ T; (f) $V_s = 400$ mV, $I_s = 200$ pA, $B = 0$ T; (g) $V_s = 400$ mV, $I_s = 200$ pA, $B = 0$ T.

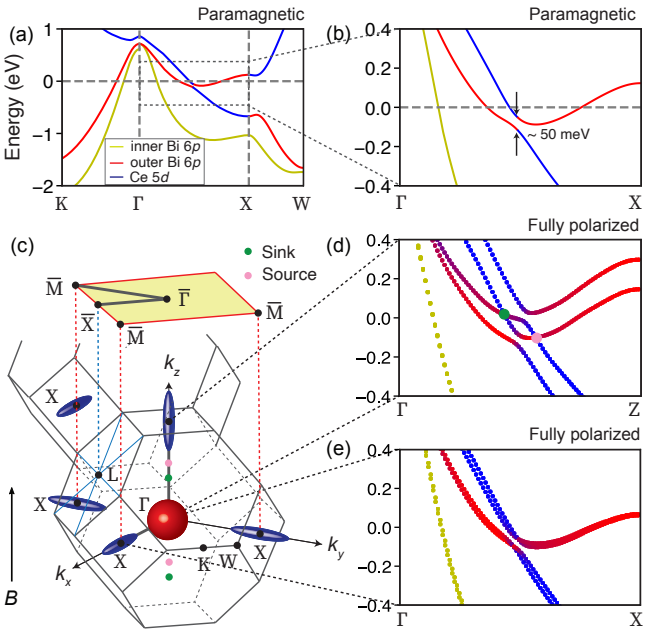

FIG. 2. (a) DFT computation of band structure along high symmetry points in the PM phase of CeBi. The outer Bi $6p$ band inverts with the Ce $5d$ band along the $\Gamma - X$ directions, which sets the nontrivial band topology in the PM phase. (b) Zoomed in plot of the band structure around the band crossing in the PM phase shows a hybridization gap of ~ 50 meV along the $\Gamma - X$ direction. (c) The Brillouin zone (BZ) of the CeBi rock-salt structure is a truncated octahedron with six square faces and eight hexagonal faces. The surface-projected BZ is square, with bulk Γ and Z points projected onto $\overline{\Gamma}$, two orthogonally-oriented bulk X points projected onto $\overline{\mathrm{M}}$, and the hexagonal-face-centered L point projected onto $\overline{\mathrm{X}}$. In the fully-polarized phase of CeBi, achieved by applying an external magnetic field along the z direction, four predicted Weyl nodes are shown as green and pink points, representing sinks and sources of Berry curvature, respectively. (d-e) DFT computation of band structure in the fully-polarized phase of CeBi, along (d) k_z and (e) k_x directions, with all the Ce moments aligned along the z direction. Along the k_z direction, two pairs of Weyl nodes are created by the splitting of the outer Bi $6p$ and Ce $5d$ bands. In contrast, along the k_x direction the band splitting is smaller and there are no predicted Weyl nodes. Note that the apparent band crossings in (e) are not Weyl crossings, as indicated by our Berry curvature calculations in Fig. 6.

and Ce $5d$ band along the k_z direction is larger than the hybridization gap size of 50 meV, there will be two pairs of Weyl nodes. We performed QPI measurements in the (++−−) phase at 0 T and in the (++++) state at 9 T along the z direction, discovering that the inner to outer Bi $6p$ scattering vector splits ~ 150 meV and the outer Bi $6p$ band splits ~ 200 meV at 9 T along the k_x direction. This large band splitting suggests that both the inner Bi $6p$ and outer Bi $6p$ bands are split by the internal magnetism and the splitting of the outer Bi $6p$ band along the k_z should be large enough to overcome the hybridization gap. In addition, we observe three sets of trivial surface states in the QPI taken in the (++++) state, matching the prediction from our surface slab calculation. Our discovery supports that Weyl nodes exist in the fully polarized CeBi.

II. METHODS

A. DFT

The bulk band structure of CeBi was calculated using the generalized-gradient approximation (GGA) as implemented in the all-electron code WIEN2K [30], with the augmented-plane-wave + local-orbitals (APW+lo) basis set. In the paramagnetic phase we treated the Ce $4f$ orbitals as core electrons. The Hubbard Coulomb interaction on Ce $4f$ electrons was incorporated to ensure a fully localized Ce $4f$ state, which also gives a total magnetic moment of $2\mu_B$/Ce, consistent with earlier studies on cerium monopnictides [27, 31, 32]. The surface electronic structure was calculated using both the direct diagonalization and the iterative Green's function method [28, 33].

B. Experiment

Single crystals of CeBi were grown by the self-flux method [27]. Samples were cleaved in cryogenic ultra

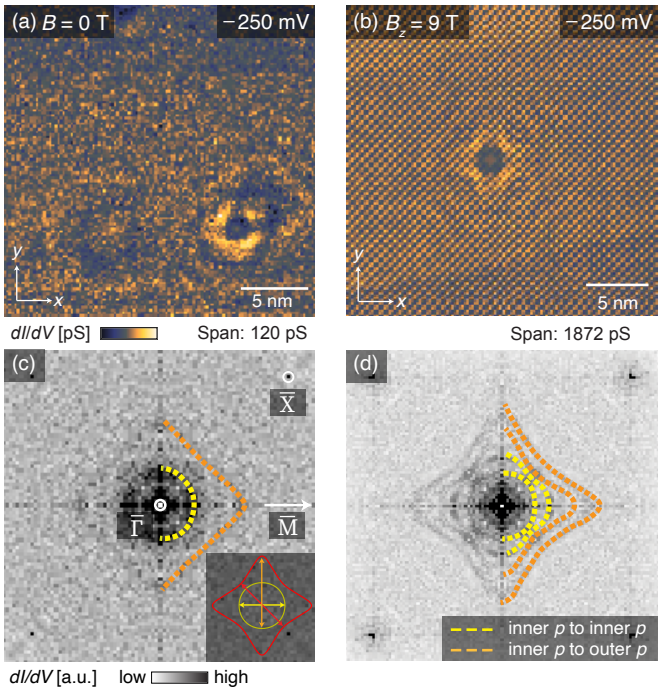

FIG. 3. (a) dI/dV map at sample bias -250 mV in the $(++--)$ phase shows the real space QPI patterns as ripples around the impurity. Setpoints: $V_s = -250$ mV, $I_s = 900$ pA, bias modulation $V_{rms} = 8.5$ mV. (b) dI/dV map at -250 mV in the $(++++)$ state. Setpoints: $V_s = 200$ mV, $I_s = 2$ nA, $V_{rms} = 7.1$ mV. (c) Fourier transform (FT) of the dI/dV map in (a) contains the scattering vector information in the QPI. The inset shows the DFT computed constant energy band contours of CeBi on the $k_z = 0$ plane in the PM phase, with double head arrows representing possible scattering vectors between the two hole-like Bi $6p$ bands. (d) FT of the dI/dV map in (b) shows the QPI scattering vectors in the $(++++)$ state. By comparing FT patterns with the DFT computed constant energy band contours and band dispersions measured by ARPES, we identify the intra-band scattering vector of the inner p (yellow) and the inner to outer p scattering vector (orange) in our QPI results. A Gaussian mask with width of 0.4 nm has been applied to the impurities in (a) and (b) to reduce the effect of the impurity form factor in the FT. The FT patterns in (c) and (d) have been 4-fold symmetrized to enhance the signal to noise. The colored dash lines overlaid in (c) and (d) are schematic drawings to highlight the identity and location of each scattering vector.

high vacuum and immediately inserted into STM head. All STM measurements were performed at $T = 4.6$ K. QPI imaging was performed in the (x, y) and (x, z) planes of the antiferromagnetic $(++--)$ phase at $B = 0$ T, and in the (x, y) plane of the fully-polarized $(++++)$ state with $B = 9$ T applied along the z direction.

III. DFT RESULTS

4 **[DFT shows there is a band inversion between the Bi $6p$ and Ce $5d$ bands in the PM phase. In the $(++++)$ state, band splitting creates two pairs of Weyl nodes along the k_z direction]**

In the PM phase, our DFT calculation shows that the band inversion between the Ce $5d$ and Bi $6p$ bands along the $\Gamma - X$ direction sets the nontrivial band topology of CeBi [Fig. 2(b)]. At the band crossing point, the hybridization between the two bands opens a gap of ~ 50 meV [Fig. 2(c)] and thus there is no Weyl node in the PM phase. This gap has been confirmed by ARPES results in the same phase [22, 24]. In the $(++++)$ state, all the Ce moments are set along the z direction. The Ce $5d$ and Bi $6p$ bands are predicted to split by ~ 100 meV along the k_z direction around the band crossing point [Fig. 2(e)]. Our DFT shows there are two band crossing points that are not gapped out by the hybridization due to the opposite eigenvalues of the symmetry operator $\sigma_{xy}T$, where σ_{xy} is the mirror operator of the xy plane and T is the time reversal operator [34, 35]. Berry curvature calculation further confirms that these are indeed Weyl nodes [Fig. 6(c)].

5 **[In the $(++++)$ state, a large band splitting ($\Delta_p > 50$ meV) is required for the Weyl nodes to exist]**

When the external magnetic field is set along the z direction, the band splitting size is larger along the k_z direction compared to perpendicular directions, as shown in Fig. 2(e-f). According to our DFT calculation, when the combined splitting of the outer Bi $6p$ band and Ce $5d$ band is larger than the hybridization gap of 50 meV, the symmetry protected band crossings form Weyl nodes. If the combined band splitting is too small, the hybridization of the bands with the same $\sigma_{xy}T$ eigenvalues would prevent the two bands that form Weyl nodes from touching each other. Therefore, it is important to quantify the band splitting experimentally to determine the band topology of CeBi in the $(++++)$ state.

IV. QPI RESULTS

6 **[Introduction to QPI]**

To study the band structure of CeBi, we took dI/dV maps at different sample bias around natural defects, which measures the local density of states map at different enrgy [Fig. 3(a-b)]. QPI standing waves appear as ripples around impurities in the dI/dV maps, which is the result of electron waves being scattered by the impurity potential. The Fourier transform (FT) of those dI/dV maps contains the scattering vector (momentum transfer) information of the QPI [Fig. 3(c-d)], which reflects the original band structure of the material.

7 **[Extract Bi $6p$ scattering vectors by comparing QPI and DFT constant energy band contours]**

To identify the scattering vectors in our dI/dV maps, we compare the FT of the real space maps with the DFT computed constant energy band contours. Here we are using the DFT calculated band structure in the PM phase to compare with our QPI results measured in the

(++−−) phase because we did not observe any signs of band folding in both the FT patterns of QPI [Fig. 3(c)] and QPI dispersion [Fig. 4(a-b)]. We attribute the scattering vector marked by the yellow dash line in Fig. 3(c) to the intra-cone scattering of the inner p band ($\boldsymbol{q}_{\rm ii}$), as that is the only band with a circular shape in DFT calculated contours. There are two possible origins for the scattering vector marked by the orange dash line: the inner p to outer p scattering ($\boldsymbol{q}_{\rm io}$) or the intra-cone scattering of the outer p band ($\boldsymbol{q}_{\rm oo}$). By comparing the energy dispersion of the orange scattering vector with the band dispersion reported by previous ARPES study [23] along the same direction [Fig. 7(a)], we conclude that it is the $\boldsymbol{q}_{\rm io}$ scattering vector.

8 **[Transition paragraph]**

With the scattering vectors identified, we are able to compare the band structure in the (++−−) and (++++) states to search for evidences of magnetism induced band splitting. Comparing Fig. 3(c-d), we notice that both the $\boldsymbol{q}_{\rm ii}$ and $\boldsymbol{q}_{\rm io}$ scattering vectors are splitting, which offers the opportunity to quantify the band splitting size by tracking the energy dispersion of those scattering vectors.

9 **[QPI result of band splitting]**

To quantify the magnetism induced band splitting in the (++++) state, we measured the energy dispersion of QPI scattering vectors by taking linecuts at different energy along the $\overline{\Gamma}-\overline{\rm M}$ and $\overline{\Gamma}-\overline{\rm X}$ directions of the FT patterns in Fig. 4(a-d). Along the $\overline{\Gamma}-\overline{\rm M}$ direction, the single $\boldsymbol{q}_{\rm io}$ scattering vector in 0 T QPI [Fig. 4(a)] splits into two scattering vectors in 9 T QPI ($\boldsymbol{q}_{\rm io1}$ and $\boldsymbol{q}_{\rm io2}$ in Fig. 4(c)), with a splitting size estimated to be $\sim$ 150 meV. A similar splitting in the $\boldsymbol{q}_{\rm ii}$ scattering vector $\sim$ 100 meV is observed along the same direction. From the splitting sizes of $\boldsymbol{q}_{\rm ii}$ and $\boldsymbol{q}_{\rm io}$, we can further derive that the splitting of the outer p band is $\sim$ 200 meV along the $\overline{\Gamma}-\overline{\rm M}$ direction, as shown in Fig. 7(b). According to our DFT calculation [Fig. 2(e-f)], the splitting of the outer p band is larger along the k_z direction compared to the k_x direction when the external magnetic field is applied along the z direction. Therefore, the lower bound of the outer Bi 6p band splitting is 200 meV along the k_z direction, which leads to the conclusion that the splitting of the outer Bi 6p band is larger than the hybridization gap of 50 meV in the (++++) state.

10 **[Surface states in the (++++) state of CeBi: SS1 and SS2 agree with DFT, but SS3 doesn't.]**

In addition to the band splitting in the bulk state scattering vectors, we have also observed three surface state scattering vectors in the (++++) state. The circular surface states SS1 and SS2 at −300 mV in Fig. 5(b) match the intra-cone scattering of the surface states SS1 and SS2 in the DFT computed surface projected spectral functions in Fig. 5(c), respectively. Notice that the SS2 centered at $\overline{\rm M}$ point in Fig. 5(c) is transfered to the $\overline{\Gamma}$ point in Fig. 5(b) as QPI measures the momentum transfer in the scattering process instead of the absolute momentum. Furthermore, the hole-like dispersion of the SS1 and SS2 are marked by the green dash lines along the $\overline{\Gamma}-\overline{\rm M}$ [Fig. 4(c)] and $\overline{\Gamma}-\overline{\rm X}$ [Fig. 4(d)] directions, showing qualitative agreement with what ARPES studies have reported in the (++−−) and paramagnetic phases [22–24].

The surface state SS3 at −200 mV in Fig. 5(a) has three main features: first, it has an arc-like shape around −200 meV; second, it has a hole-like dispersion, which means its momentum transfer $\boldsymbol{q}$ becomes smaller at higher energy; third, its pocket size becomes smaller at higher energy. Although the overall shape of the surface state SS3 measured by QPI in Fig. 5(a) matches the intra-cone scattering of the SS3 computed by DFT in Fig. 5(c), the DFT computed SS3 displays an electron-like dispersion, which is opposite to that of the QPI measured SS3. If we consider the inter-cone scattering of the SS3 in Fig. 5(c) to be the origin of the QPI measured SS3, the hole-like dispersion can be explained. However, neither the shape of the scattering pattern nor the energy dependence of the pocket size will agree between QPI and DFT. Therefore, the arc-like SS3 observed in QPI cannot be explained by any bands predicted by our DFT.

The agreement between our observed surface states scattering vectors in QPI and calculated surface state spectral functions for SS1 and SS2 verifies our theoretical prediction about the surface states in the (++++) state, and further supports that Weyl nodes and Fermi arcs exist in the fully polarized CeBi as predicted in this and previous work [28].

11 **[Discussion 1: CeBi should be a tunable Weyl semimetal]**

The absence of band splitting in the (++−−) phase and the large band splitting in the (++++) state show that the intrinsic magnetism is playing an important role in band splitting, and it is possible to control the band topology of CeBi with the external magnetic field. With 9 T external magnetic field, the Zeeman splitting of the Ce 5d and Bi 6p bands is estimated to be $\sim$ 1 meV if we take the experimental value of $g_{\rm Ce} = 2$, which is much smaller than our observed band splitting. This means that the internal magnetism is the key factor in creating a large band splitting in CeBi. Our measurements support that CeBi is a tunable magnetic Weyl semimetal as it is possible to tune the Weyl properties by driving the material between the (++−−) and (++++)phases.

V. CONCLUSION

In conclusion, our QPI measurements of CeBi in the (++−−) and (++++) states support the theoretical prediction that CeBi hosts Weyl nodes in the (++++) state and CeBi is a tunable magnetic Weyl semimetal. We discover large band splitting in both the inner Bi 6p and outer 6p bands, which suggests that there are Weyl nodes in the (++++) state of CeBi. The absence of band splitting in the (++−−) phase further suggests that CeBi is a tunable magnetic Weyl semimetal and it is possible to tune the band topology of CeBi between different magnetic phases. The observation of surface states in the

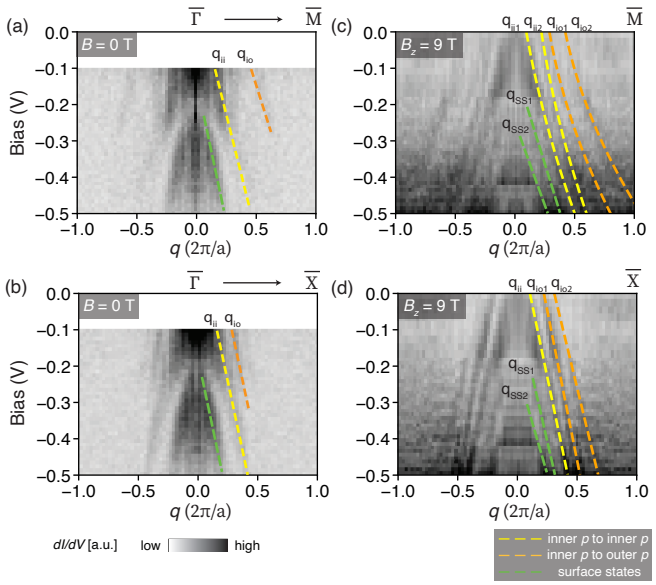

FIG. 4. (a-b) Dispersions of QPI scattering vectors along (a) $\overline{\Gamma}-\overline{\mathrm{M}}$ and (b) $\overline{\Gamma}-\overline{\mathrm{X}}$ directions in the (++−−) phase (4.6 K, 0 T, $V_\mathrm{s}=-100$ mV with the current set point adapted for each bias to maintain $I_\mathrm{s}=800$ pA, $V_\mathrm{rms}=7.1$ mV). The dash lines plotted on top of the data are schematic drawing indicating the identity and location of scattering vectors. (c-d) Similar dispersions in the (++++) state (4.6 K, 9 T along the z direction, $V_\mathrm{s}=200$ mV, $I_\mathrm{s}=2$ nA, $V_\mathrm{rms}=7.1$ mV) are shown along (c) $\overline{\Gamma}-\overline{\mathrm{M}}$ and (d) $\overline{\Gamma}-\overline{\mathrm{X}}$ directions. The inner p to outer p scattering vectors ($\boldsymbol{q}_{\mathrm{io}1}$ and $\boldsymbol{q}_{\mathrm{io}2}$) show a splitting $\sim$ 150 meV along both directions. The inner p scattering vectors ($\boldsymbol{q}_{\mathrm{ii}1}$ and $\boldsymbol{q}_{\mathrm{ii}2}$) show a splitting $\sim$ 100 meV only along the $\overline{\Gamma}-\overline{\mathrm{M}}$ direction. All the linecuts in this figure are taken from 4-fold symmetrized FT patterns to enhance signal to noise ratio. The QPI dispersion plots in (c) and (d) have been normalized at each q-value for better visualization.

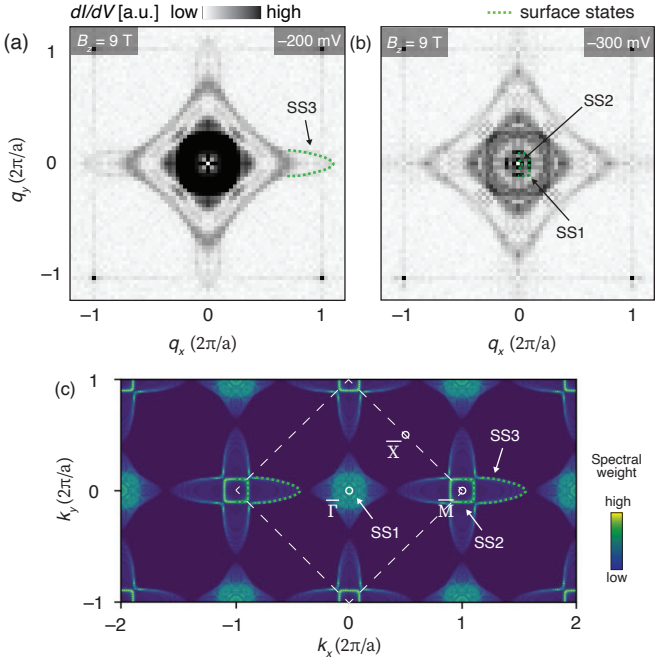

FIG. 5. (a-b) FT of the dI/dV maps at (a) −200 mV and (b) −300 mV show the signatures of surface states. The map was set up at V_s =200 mV, with the current setpoint $I_\mathrm{s}=2$ nA and bias modulation $V_\mathrm{rms}=7.1$ mV. During the dI/dV map, the sample was kept at 4.6 K with a 9 T external magnetic field along the z direction. (c) Surface projected spectral functions calculated in the (++++) state show three sets of surface states, with two centered at the $\overline{\mathrm{M}}$ point (SS2 and SS3) and one centered at the $\overline{\Gamma}$ point (SS1). In this calculation, the magnetic moments of Ce atoms are aligned along the z direction. The white dash lines enclose the first surface Brillouin zone. The surface states SS1 and SS2 agree between (a-b) QPI and (c) DFT calculation. However, the SS3 in (a) QPI does not match neither the intra-cone nor the inter-cone scattering of SS3 predicted by DFT in (c). A Gaussian mask with width of 0.4 nm has been applied at the impurity center in the real space map of (a) and (b) to reduce the effect of the impurity center in the Fourier transform. The FT patterns in (a) and (b) has been 4-fold symmetrized to enhance the signal to noise contrast.

(++++) state verifies our surface slab calculation in the same phase. Our results call for future studies on how the separation of Weyl nodes and Weyl properties change between different magnetic phases of CeBi.

Appendix A: Berry curvature calculation

In the (++++) state, the DFT computed band structure along the k_z and k_x directions [Fig. 6(a-b)] both display band crossing features. To determine whether these band crossings are Weyl nodes, we further calculated the Berry curvature vector field. Fig. 6(c) shows the Berry curvature vector field on the $\Gamma-\mathrm{X}-\mathrm{Z}$ plane in the first Brillouin for the black bands in Fig 6(a-b), with all the Ce moments set along the z direction. Two divergences in the vector field are identified along the $-\mathrm{Z}-\Gamma-\mathrm{Z}$ line at the band crossing points, with one node identified as a sink (green) and the other as a source (pink) of topological charge, which confirms that the two band crossings along the k_z direction [Fig. 6(a)] are indeed Weyl nodes. In contrary, there is no such sink or source behavior along the $\Gamma-\mathrm{X}$ direction, meaning that the band crossings along the k_x direction [Fig. 6(b)] are not Weyl nodes. From the Berry curvature calculation, we can conclude that there are two pairs of Weyl nodes along the k_z direction and no Weyl node along the k_x direction when the Ce moments are aligned along the z direction.

Appendix B: Compare QPI with DFT and ARPES

To determine the origins of the scattering vectors in our QPI, in Fig. 7(a), we plot the energy dispersion of QPI from Fig. 4(a) as cross marks on top of the band dispersion measured by ARPES [23] in the same mag-

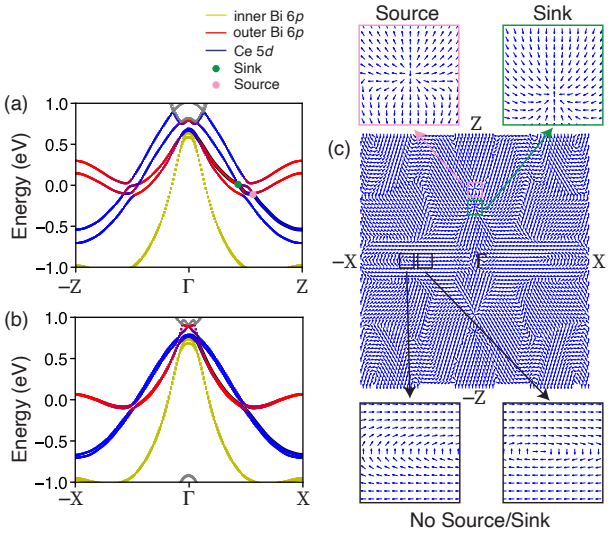

FIG. 6. **Berry curvature calculation in the fully polarized CeBi** (a-b) DFT computed band structure of CeBi along the (a) k_z and (b) k_x directions in the (++++) state. All the Ce magnetic moments are aligned along the z direction. (c) Calculated Berry curvature vector field on the xz plane for the black marked bands in (a) and (b). The Weyl nodes are marked in green (pink) indicating they are a sink (source) of Berry flux. There are sink and source behaviors in the Berry curvature vector field along the $\Gamma - Z$ direction, confirming that the two band crossing points in (a) are indeed Weyl nodes. Although there are also band crossing points in (b), there is no sink or source behavior along the $\Gamma - X$ direction, meaning that the band crossing points in (b) are not Weyl nodes. This figure is adapted from [28].

netic phase. Here we use the relation between momentum transfer $\boldsymbol{q}$ and absolute momentum $\boldsymbol{k}$ that $\boldsymbol{q} = 2\boldsymbol{k}$ to convert the QPI energy dispersion to the same unit as the ARPES measured band dispersion. We notice that there is a reasonably good agreement for the yellow scattering vector in QPI and the inner p bands measured by ARPES. For the orange scattering vector, it does not match any bands in the ARPES. Instead, it is in the middle of the inner p and outer p bands, which means that its dispersion agrees with the inner to outer p scattering vector. Therefore, the yellow and orange scattering vectors in Fig. 4(a) originate from the intra-cone scattering of inner p band and inner to outer p scattering, respectively.

In Fig. 7(b-c), we discuss about how scattering vectors change with band splitting. Each scattering vector in the (++−−) phase should become four scattering vectors ($\boldsymbol{q}_{\rm io1}$ to $\boldsymbol{q}_{\rm io4}$) in the (++++) state with band splitting. Among those four scattering vectors, $\boldsymbol{q}_{\rm io3}$ and $\boldsymbol{q}_{\rm io4}$ vectors require flipping of electron spins in the scattering process and thus have suppressed intensity compared to the $\boldsymbol{q}_{\rm io1}$ and $\boldsymbol{q}_{\rm io2}$ vectors. In our experiment, we observe that each scattering vector in the (++−−) phase splits into two scattering vectors in the (++++) state, which can be attributed to the two spin non-flipping scattering vectors.

In addition, it can be seen that the splitting energy of the inner to outer p scattering vector $\boldsymbol{q}_{\rm io}$ in the (++++) state equals the averaged splitting energy of the inner p scattering vector $\boldsymbol{q}_{\rm ii}$ and the outer p scattering vector $\boldsymbol{q}_{\rm oo}$ in the same state.

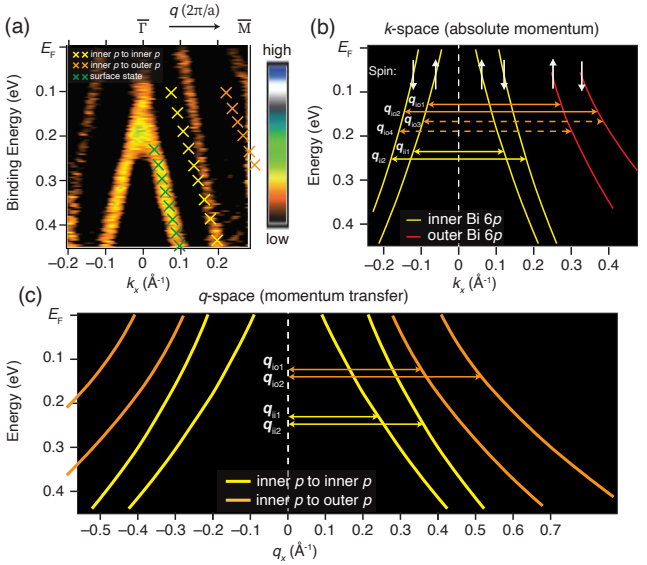

FIG. 7. **Comparison between QPI and ARPES** (a) Comparison of band dispersion measured by ARPES [23] on the (001) surface in the (++−−) phase and QPI in the same phase. The ARPES result (background) was measured at 6 K, 0 T. The colored cross marks on top of ARPES results indicate band dispersion measured by QPI, replicated from the dash lines in Fig. 4(a). (b-c) Relation between k space (absolute momentum) and q space (momentum transfer) in QPI measurements. (b) Band structure in the (++++) state extracted from QPI dispersion. The inner Bi 6p band is obtained from the yellow dash lines in Fig. 4(c) with the relation $\boldsymbol{q}_{\rm ii} = 2\boldsymbol{k}_{\rm i}$. The outer Bi 6$p$ band is obtained by back-tracking the yellow and orange dash lines in Fig. 4(c) with the relation $\boldsymbol{q}_{\rm io} = \boldsymbol{k}_{\rm o} - \boldsymbol{k}_{\rm i}$, as the orange double head vectors are the inter-band scattering vectors between the inner and outer Bi 6p bands. The solid orange double arrow vectors ($\boldsymbol{q}_{\rm io1}$ and $\boldsymbol{q}_{\rm io2}$) represent spin non-flipping scattering vectors between the inner and outer Bi 6p bands, while dash orange double arrow vectors ($\boldsymbol{q}_{\rm io3}$ and $\boldsymbol{q}_{\rm io4}$) represent spin-flipping scattering vectors. The solid yellow double arrow vectors ($\boldsymbol{q}_{\rm ii1}$ and $\boldsymbol{q}_{\rm ii2}$) represent spin non-flipping intra-cone scattering vectors of the inner Bi 6p band. (c) Schematic drawing of the QPI scattering vectors in the momentum transfer space (q space), with the yellow and orange lines replicated from Fig. 4(c). The double arrow vectors here are replicated from (b). In the q space, all the pockets are centered at the Γ point as the scattering vector indicates the relative difference between the momentum of the final state and initial state.

Appendix C: Data consistency check

To eliminate the effect of the high intensity impurity centers, we apply Gaussian masks on the impurities. We

Map	Bias (mV)	Setpoint (nA)	Modulation (mV)	B (T)	Figures
1	−100	0.8	7.1	0	3 (a), (c) 4 (a-b) 8 (a1-a2) 9 (b1-b6)
2	−250	0.9	8.5	0	9 (a1-a6)
3	200	2	7.1	9	3 (b), (d) 4 (c-d) 8 (a3-a4) 10 (a1-b6)
4	−200	4	7.1	9	10 (c1-d6)
5	200	2	7.1	9	5 (a-b)

TABLE I. Setup parameters for all the dI/dV maps used in this work.

multiply $\mathrm{G}(\mathbf{r}) = 1 - \exp(-(\mathbf{r} - \mathbf{r_0})^2/w^2)$ at the center of impurities, where $\mathbf{r_0}$ is the location of the impurity center and w is the width of the Gaussian mask [36]. In Fig. 8, we show the effect of the Gaussian mask on the FT pattern of QPI. Comparing Fig. 8(b1-b2) and (b3-b4), the Gaussian masks do not change the positions of QPI scattering vector. Instead, it reveals fine structures in QPI better by suppressing the large intensity induced by impurity center.

In Fig. 9, to show that the $\boldsymbol{q}_{\mathrm{ii}}$ and $\boldsymbol{q}_{\mathrm{io}}$ scattering vectors in the $(++--)$ phase [Fig. 4(a-b)] originate from the band structure instead of impurity form factor, we have cropped around multiple impurities in different areas to show that those two scattering vectors also present around other impurities. This can be seen from the band dispersion comparison between Fig. 9(a3 and b3). Although the intensity of scattering vectors changes across different impurities, the wavevectors of the yellow and orange scattering channels appear similar in all the three dispersion plots.

Similarly, in Fig. 10, to verify that the QPI measured splitting features in the $(++++)$ state are induced by the band splitting, we show that similar splitting features occur in the QPI dispersion and FT patterns in several areas with different impurities, which rules out the possibility of impurity form factor. Although the splitting feature occurs in all of the four areas, there are energy shifts between the same scattering vectors across areas Fig. 10(a1)-(d1). This is probably because those four areas contain different types of impurities, which can slightly change the band position around them due to the local doping effect.

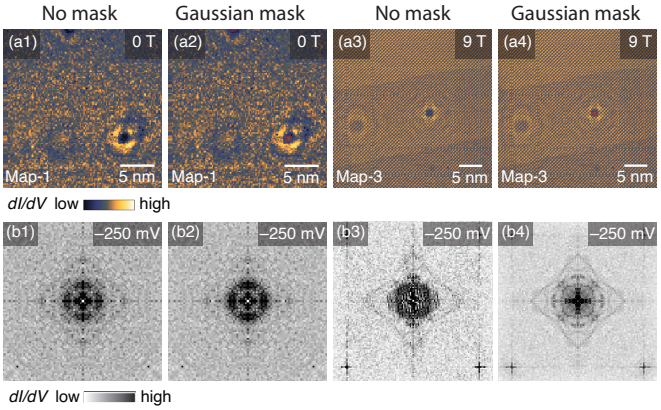

FIG. 8. **The effect of Gaussian mask** (a1-a2) Real space dI/dV map at −250 mV and 0 T (a1) with and (a2) without Gaussian mask of 0.4 nm wide. (a3-a4) Real space dI/dV map at −250 mV and 9 T (a3) with and (a4) without Gaussian mask of 0.4 nm wide. (b1-b4) FT of the real space dI/dV maps in (a1-a4). The data in (b2) has been 2-fold symmetrized and data in (b4) has been 4-fold symmetrized to enhance the signal to noise ratio. Setup conditions for the maps are summarized in Table I.

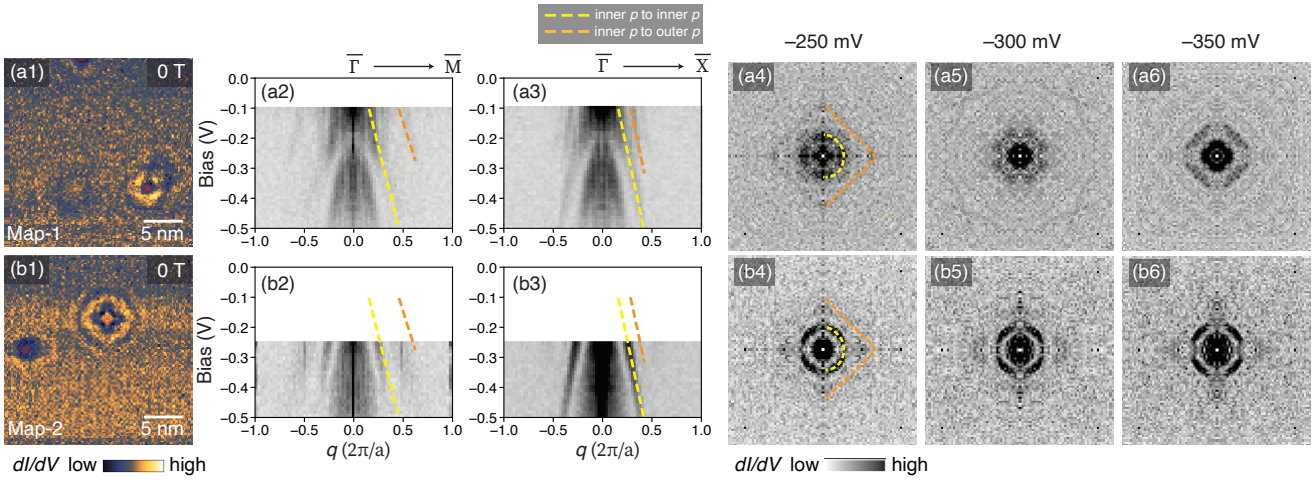

FIG. 9. **Data consistency check for the (++−−) phase (with Gaussian mask)** (a1) Real space dI/dV map at −250 mV. (a2-a3) QPI dispersions along the (a2) $\overline{\Gamma}-\overline{\mathrm{M}}$ and (a3) $\overline{\Gamma}-\overline{\mathrm{X}}$ directions. The $\boldsymbol{q}_{\mathrm{ii}}$ (yellow dash line) and $\boldsymbol{q}_{\mathrm{io}}$ (orange dash line) scattering vectors in Fig. 4(a-b) are plotted on top of the QPI dispersions in (a2) and (a3), respectively. (a4-a6) FT of the real space dI/dV maps at (a4) −250 mV, (a5) −300 mV, and (a6) −350 mV. Similar analysis has been done in (b1-b6) a different area. The colored dash lines are identical for all the $\overline{\Gamma}-\overline{\mathrm{M}}$ (a2 and b2) and $\overline{\Gamma}-\overline{\mathrm{X}}$ (a3 and b3) directions. The colored half contours are identical for (a4) and (b4), which are replicated from Fig. 3(c). To remove the low frequency noise induced by the high intensity impurity centers, we have applied Gaussian masks with a width of 0.4 nm (red circle in (a1) and (b1)) in the real space maps. Drift induced by the piezoelectric relaxation and temperature change has been removed in the real space maps. All the FT patterns from map-1 in this figure have been 2-fold symmetrized to enhance the signal to noise ratio. All the FT patterns from map-2 have been 4-fold symmetrized. Setup conditions for the maps are summarized in Table I.

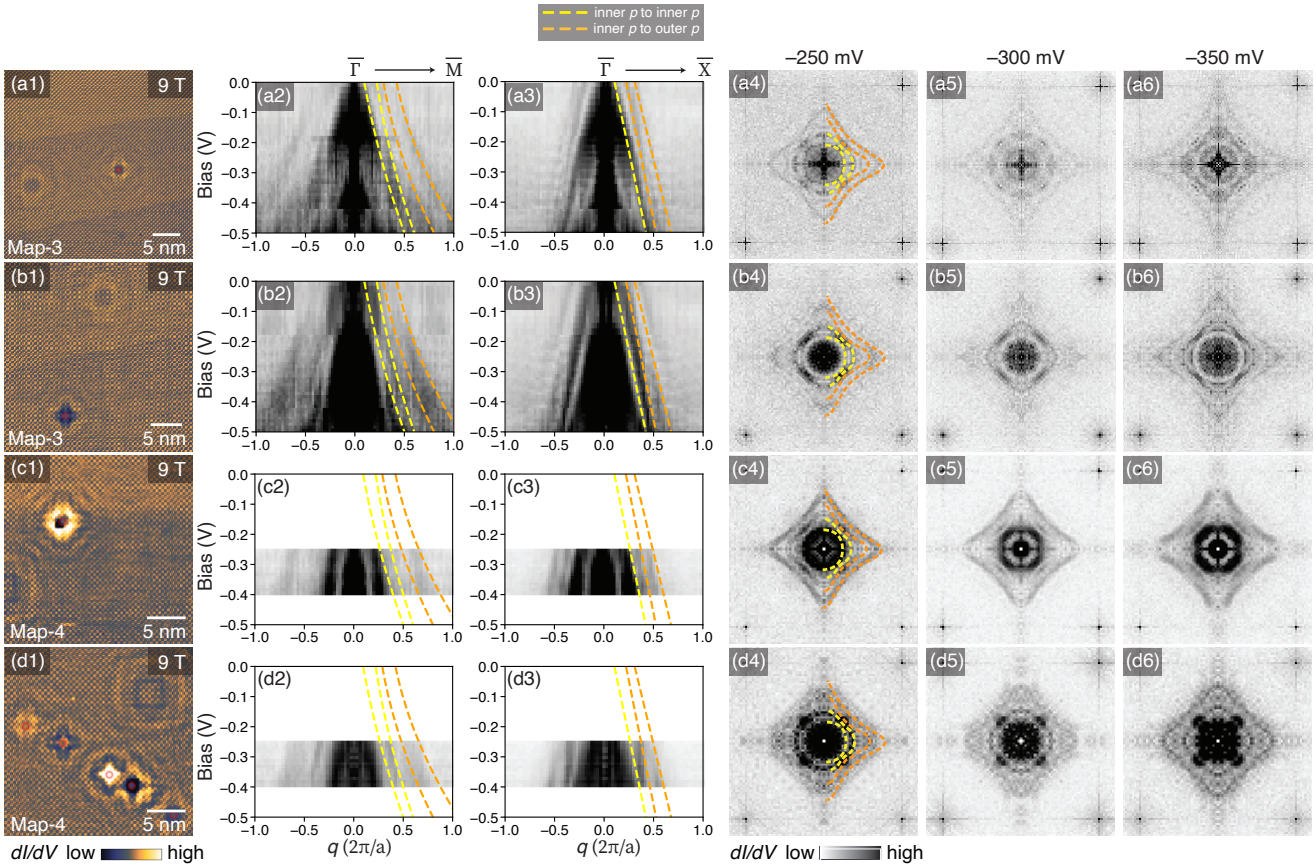

FIG. 10. **Data consistency check for the (++++) state (with Gaussian mask)** (a1) Real space dI/dV map at −250 mV is taken in the (++++) state with 9 T out-of-plane external magnetic field applied. (a2-a3) QPI dispersions along the (a2) $\overline{\Gamma}-\overline{\mathrm{M}}$ and (a3) $\overline{\Gamma}-\overline{\mathrm{X}}$ directions. The $\boldsymbol{q}_{\mathrm{ii1}}$ and $\boldsymbol{q}_{\mathrm{ii2}}$ (yellow dash lines), $\boldsymbol{q}_{\mathrm{io1}}$ and $\boldsymbol{q}_{\mathrm{io2}}$ (orange dash lines) scattering vectors in Fig. 4(c-d) are plotted on top of the QPI dispersions in (a2) and (a3), respectively. (a4-a6) FT patterns of QPI at (a4) −250 mV, (a5) −300 mV, and (a6) −350 mV. Similar analysis has been done in (b1-b6), (c1-c6), and (d1-d6) for three different areas. The colored dash lines are identical for all the $\overline{\Gamma}-\overline{\mathrm{M}}$ (a2, b2, c2, d2) and $\overline{\Gamma}-\overline{\mathrm{X}}$ (a3, b3, c3, d3) directions. The colored half contours are identical for (a4), (b4), (c4) and (d4), which are replicated from Fig. 3(d). To remove the low frequency noise induced by the high intensity impurity centers, we have applied Gaussian masks with a width of 0.4 nm (red circle in (a1), (b1), (c1) and (d1) in the real space maps. Drift induced by piezo relaxation and temperature change has been removed in the real space map. All the FT patterns in this figure have been 4-fold symmetrized to enhance the signal to noise ratio. Setup conditions for the maps are summarized in Table I.

[1] N. P. Armitage, E. J. Mele, and A. Vishwanath, Weyl and Dirac semimetals in three-dimensional solids, Reviews of Modern Physics **90**, 015001 (2018).

[2] F. Arnold, C. Shekhar, S. C. Wu, Y. Sun, R. D. D. Reis, N. Kumar, M. Naumann, M. O. Ajeesh, M. Schmidt, A. G. Grushin, J. H. Bardarson, M. Baenitz, D. Sokolov, H. Borrmann, M. Nicklas, C. Felser, E. Hassinger, and B. Yan, Negative magnetoresistance without well-defined chirality in the Weyl semimetal TaP, Nature Communications **7**, 11615 (2016).

[3] X. Huang, L. Zhao, Y. Long, P. Wang, D. Chen, Z. Yang, H. Liang, M. Xue, H. Weng, Z. Fang, X. Dai, and G. Chen, Observation of the chiral-anomaly-induced negative magnetoresistance: In 3D Weyl semimetal TaAs, Physical Review X **5**, 031023 (2015).

[4] T. Suzuki, R. Chisnell, A. Devarakonda, Y. T. Liu, W. Feng, D. Xiao, J. W. Lynn, and J. G. Checkelsky, Large anomalous Hall effect in a half-Heusler antiferromagnet, Nature Physics **12**, 1119 (2016).

[5] E. Liu, Y. Sun, N. Kumar, L. Muechler, A. Sun, L. Jiao, S. Y. Yang, D. Liu, A. Liang, Q. Xu, J. Kroder, V. Süß, H. Borrmann, C. Shekhar, Z. Wang, C. Xi, W. Wang, W. Schnelle, S. Wirth, Y. Chen, S. T. Goennenwein, and C. Felser, Giant anomalous Hall effect in a ferromagnetic kagome-lattice semimetal, Nature Physics **14**, 1125 (2018).

[6] A. Sakai, Y. P. Mizuta, A. A. Nugroho, R. Sihombing, T. Koretsune, M. T. Suzuki, N. Takemori, R. Ishii, D. Nishio-Hamane, R. Arita, P. Goswami, and S. Nakatsuji, Giant anomalous Nernst effect and quantum-critical scaling in a ferromagnetic semimetal, Nature Physics **14**, 1119 (2018).

[7] M. Ikhlas, T. Tomita, T. Koretsune, M. T. Suzuki, D. Nishio-Hamane, R. Arita, Y. Otani, and S. Nakatsuji, Large anomalous Nernst effect at room temperature in a chiral antiferromagnet, Nature Physics **13**, 1085 (2017).

[8] Y. Tokura, M. Kawasaki, and N. Nagaosa, Emergent functions of quantum materials, Nature Physics **13**, 1056 (2017).

[9] L. Šmejkal, Y. Mokrousov, B. Yan, and A. H. MacDonald, Topological antiferromagnetic spintronics, Nature Physics **14**, 242 (2018).

[10] E. H. da Silva Neto, "Weyl"ing away time-reversal symmetry, Science **365**, 1248 (2019).

[11] K. Kuroda, T. Tomita, M.-T. Suzuki, C. Bareille, A. A. Nugroho, P. Goswami, M. Ochi, M. Ikhlas, M. Nakayama, S. Akebi, R. Noguchi, R. Ishii, N. Inami, K. Ono, H. Kumigashira, A. Varykhalov, T. Muro, T. Koretsune, R. Arita, S. Shin, T. Kondo, and S. Nakatsuji, Evidence for magnetic Weyl fermions in a correlated metal, Nature Materials **16**, 1090 (2017).

[12] N. Morali, R. Batabyal, P. K. Nag, E. Liu, Q. Xu, Y. Sun, B. Yan, C. Felser, N. Avraham, and H. Beidenkopf, Fermi-arc diversity on surface terminations of the magnetic Weyl semimetal $Co_3Sn_2S_2$, Science **365**, 1286 (2019).

[13] D. F. Liu, A. J. Liang, E. K. Liu, Q. N. Xu, Y. W. Li, C. Chen, D. Pei, W. J. Shi, S. K. Mo, P. Dudin, T. Kim, C. Cacho, G. Li, Y. Sun, L. X. Yang, Z. K. Liu, S. S. P. Parkin, C. Felser, and Y. L. Chen, Magnetic Weyl semimetal phase in a kagomé crystal, Science **365**, 1282 (2019).

[14] Discovery of topological Weyl fermion lines and drumhead surface states in a room temperature magnet, Science **365**, 1278 (2019).

[15] J. Xiong, S. K. Kushwaha, T. Liang, J. W. Krizan, M. Hirschberger, W. Wang, R. J. Cava, and N. P. Ong, Evidence for the chiral anomaly in the Dirac semimetal Na_3Bi, Science **250**, 413 (2015).

[16] C. L. Zhang, S. Y. Xu, C. M. Wang, Z. Lin, Z. Z. Du, C. Guo, C. C. Lee, H. Lu, Y. Feng, S. M. Huang, G. Chang, C. H. Hsu, H. Liu, H. Lin, L. Li, C. Zhang, J. Zhang, X. C. Xie, T. Neupert, M. Z. Hasan, H. Z. Lu, J. Wang, and S. Jia, Magnetic-tunnelling-induced Weyl node annihilation in TaP, Nature Physics **13**, 979 (2017).

[17] K. Manna, L. Muechler, T. H. Kao, R. Stinshoff, Y. Zhang, J. Gooth, N. Kumar, G. Kreiner, K. Koepernik, R. Car, J. Kübler, G. H. Fecher, C. Shekhar, Y. Sun, and C. Felser, From colossal to zero: Controlling the anomalous Hall effect in magnetic Heusler compounds via Berry curvature design, Physical Review X **8**, 041045 (2018).

[18] I. Belopolski, T. A. Cochran, X. Liu, Z. J. Cheng, X. P. Yang, Z. Guguchia, S. S. Tsirkin, J. X. Yin, P. Vir, G. S. Thakur, S. S. Zhang, J. Zhang, K. Kaznatcheev, G. Cheng, G. Chang, D. Multer, N. Shumiya, M. Litskevich, E. Vescovo, T. K. Kim, C. Cacho, N. Yao, C. Felser, T. Neupert, and M. Z. Hasan, Signatures of Weyl fermion annihilation in a correlated kagome magnet, Physical Review Letters **127**, 256403 (2021).

[19] D. F. Liu, Q. N. Xu, E. K. Liu, J. L. Shen, C. C. Le, Y. W. Li, D. Pei, A. J. Liang, P. Dudin, T. K. Kim, C. Cacho, Y. F. Xu, Y. Sun, L. X. Yang, Z. K. Liu, C. Felser, S. S. Parkin, and Y. L. Chen, Topological phase transition in a magnetic Weyl semimetal, Physical Review B **104**, 205140 (2021).

[20] X. Duan, F. Wu, J. Chen, P. Zhang, Y. Liu, H. Yuan, and C. Cao, Tunable electronic structure and topological properties of LnPn (Ln=Ce, Pr, Sm, Gd, Yb; Pn=Sb, Bi), Communications Physics **1**, 71 (2018).

[21] N. Alidoust, A. Alexandradinata, S.-Y. Xu, I. Belopolski, S. K. Kushwaha, M. Zeng, M. Neupane, G. Bian, C. Liu, D. S. Sanchez, P. P. Shibayev, H. Zheng, L. Fu, A. Bansil, H. Lin, R. J. Cava, and M. Z. Hasan, A new form of (unexpected) Dirac fermions in the strongly-correlated cerium monopnictides, , 1604.08571 (2016), arXiv:1604.08571.

[22] K. Kuroda, M. Ochi, H. S. Suzuki, M. Hirayama, M. Nakayama, R. Noguchi, C. Bareille, S. Akebi, S. Kunisada, T. Muro, M. D. Watson, H. Kitazawa, Y. Haga, T. K. Kim, M. Hoesch, S. Shin, R. Arita, and T. Kondo, Experimental determination of the topological phase diagram in cerium monopnictides, Physical Review Letters **120**, 86402 (2018).

[23] H. Oinuma, S. Souma, K. Nakayama, K. Horiba, H. Kumigashira, M. Yoshida, A. Ochiai, T. Takahashi, and T. Sato, Unusual change in the Dirac-cone energy band upon a two-step magnetic transition in CeBi, Physical Review B **100**, 125122 (2019).

[24] P. Li, Z. Wu, F. Wu, C. Cao, C. Guo, Y. Wu, Y. Liu, Z. Sun, C.-M. Cheng, D.-S. Lin, F. Steglich, H. Yuan, T.-C. Chiang, and Y. Liu, Tunable electronic structure and

surface states in rare-earth monobismuthides with partially filled f shell, Physical Review B **98**, 085103 (2018).
[25] F. Hulliger, M. Landolt, H. R. Ott, and R. Schmelczer, Low-temperature magnetic phase transitions of CeBi and CeSb, Journal of Low Temperature Physics **20**, 269 (1975).
[26] H. Bartholin, P. Burlet, S. Quezel, J. Rossat-Mignod, and O. Vogt, Hydrostatic pressure effects and neutron diffraction studies of CeBi phase diagram, Le Journal de Physique Colloques **40**, C5 (1979).
[27] B. Kuthanazhi, N. H. Jo, L. Xiang, S. L. Bud'ko, and P. C. Canfield, Magnetisation and magneto-transport measurements on CeBi single crystals, Philosophical Magazine **0**, 1 (2021).
[28] Z. Huang, C. Lane, C. Cao, G. X. Zhi, Y. Liu, C. E. Matt, B. Kuthanazhi, P. C. Canfield, D. Yarotski, A. J. Taylor, and J. X. Zhu, Prediction of spin polarized Fermi arcs in quasiparticle interference in CeBi, Physical Review B **102**, 235167 (2020).
[29] C. E. Matt, Y. Liu, H. Pirie, N. C. Drucker, N. H. Jo, B. Kuthanazhi, Z. Huang, C. Lane, J.-X. Zhu, P. C. Canfield, and J. E. Hoffman, Spin-polarized imaging of strongly interacting fermions in the ferrimagnetic state of the Weyl candidate CeBi, Physical Review B **105**, 085134 (2022).
[30] P. Blaha, K. Schwarz, G. K. H. Madsen, D. Kvasnicka, J. Luitz, R. Laskowsk, F. Tran, and L. Marks, Wien2k: An augmented plane wave plus local orbitals program for calculating crystal properties (2019).
[31] A. I. Liechtenstein, V. P. Antropov, B. N. Harmon, and E. Ed, Electronic structure and magneto-optical effects in CeSb, Physical Review B **49**, 15 (2016).
[32] C. Guo, C. Cao, M. Smidman, F. Wu, Y. Zhang, F. Steglich, F. C. Zhang, and H. Yuan, Possible Weyl fermions in the magnetic kondo system CeSb, npj Quantum Materials **2**, 39 (2017).
[33] M. P. L. Sancho, J. M. L. Sancho, J. M. L. Sancho, and J. Rubio, Highly convergent schemes for the calculation of bulk and surface green functions, Journal of Physics F **15**, 851 (1985).
[34] C. Bradley and A. Cracknell, *The Mathematical Theory of Symmetry in Solids* (Oxford University Press, Cambridge, 1972).
[35] M. I. Aroyo, A. Kirov, C. Capillas, J. M. Perez-Mato, , and H. Wondratschek, Bilbao crystallographic server. II. representations of crystallographic point groups and space groups, Acta Crystallographica A **62**, 115 (2006).
[36] H. Pirie, Y. Liu, A. Soumyanarayanan, P. Chen, Y. He, M. M. Yee, P. F. Rosa, J. D. Thompson, D. J. Kim, Z. Fisk, X. Wang, J. Paglione, D. K. Morr, M. H. Hamidian, and J. E. Hoffman, Imaging emergent heavy Dirac fermions of a topological Kondo insulator, Nature Physics **16**, 52 (2020).